Proceedings of the 1st Global Power and Propulsion Forum
GPPF 2017
Jan 16-18, 2014, Zurich, Switzerland
www.pps.global

GPPF-2017-83

COMBUSTION REGIMES IN SEQUENTIAL COMBUSTORS

Oliver Schulz
CAPS Laboratory,
Mechanical and Process Engineering Dept.
ETH Zürich, 8092, Zürich, Switzerland
Email: oschulz@ethz.ch

Nicolas Noiray
CAPS Laboratory,
Mechanical and Process Engineering Dept.
ETH Zürich, 8092, Zürich, Switzerland
Email: noirayn@ethz.ch

ABSTRACT

This numerical study compares the combustion process of a gas turbine sequential combustor at atmospheric and high pressure (10 bar) conditions. Flame propagation is found to be the driving combustion regime at 1 bar, whereas at high pressure autoignition dominates. The transition from propagation to autoignition is mapped over a range of unburned gas temperature and pressure based on 1-D flame simulations. A new Analytically Reduced Chemistry (ARC) mechanism for methane/air combustion at high pressure with 16 transported species is obtained to perform compressible 3-D Large Eddy Simulation (LES) with the Dynamic Thickened Flame model (DTF).

INTRODUCTION

Thermoacoustic instabilities are one of the major challenges in gas turbine engineering, especially at high pressure and lean conditions [1, 2]. They can appear in almost every combustion system resulting from a constructive interaction between acoustic pressure and unsteady heat release rates transmitted from the flame. Most of the laboratory research is done with setups operating at atmospheric pressure, such as e.g. [3–12]. This numerical study compares combustion processes in a second stage sequential combustion system, or also referred to as axial staging concept [13–15], at atmospheric and high pressure (10 bar).

Fuel is injected into vitiated hot gas coming from a first stage swirled flame [16] and mixing temperatures range from about 1200 K to 1400 K. In these operating conditions experimental data such as flame speeds are lacking. As reviewed by Ranzi et al. [17] experimental data for laminar flame speeds s_L for methane/air combustion is available only up to an unburned gas temperature of 400 K [18]. Turbulent flame speeds were measured up to 770 K and 14 bar [19]. To the authors knowledge no data is available for vitiated flow conditions. Nevertheless there are several studies with conditions closer to the ones found in engines, such as [10, 20, 21]. In the well documented lifted flame experiment of Cabra et al. [20] an extensive number of numerical studies, e.g. [20, 22–27] identified flame propagation and autoignition burning regimes. In regions dominated by propagation one can detect unburned mixing temperatures ranging from approximately 1150 K to 1300 K. These studies show good agreements with experimental data, which indicates that the used methane/air chemistry schemes can be applied up to these temperatures. The atmospheric Cabra experiment features a cold methane/air jet injected into a hot vitiated coflow where turbulence chemistry interactions are expected to be similar to the sequential burner. Propagation and autoignition burning regimes coexist and the dominant flame stabilisation mechanism has been characterised as autoignition (e.g. [22–24]).

The aim of this study is to identify the dominant combustion mechanisms of a sequential burner at 1 and 10 bar. It investigates if the coexistence of propagation and autoignition applies for this configuration. Based on 1-D flame simulations it also examines how the combustion process changes with increasing pressure closer to engine conditions.

CONFIGURATION AND NUMERICAL SETUP

The Sequential Burner

A sketch of the configuration is shown in Fig. 1a. Only the second stage of the sequential combustion system is simulated. Perfectly premixed first stage combustion products diluted with additional fresh air at a velocity of 65 m/s are imposed at the domain inlet. The hot gas temperature is set to 1450 K at 1 bar and is decreased to 1300 K at 10 bar with the aim of having comparable flame lengths. One might argue that inlet temperatures should be equal to investigate the influence of pressure. It is not possible to find such a condition for this

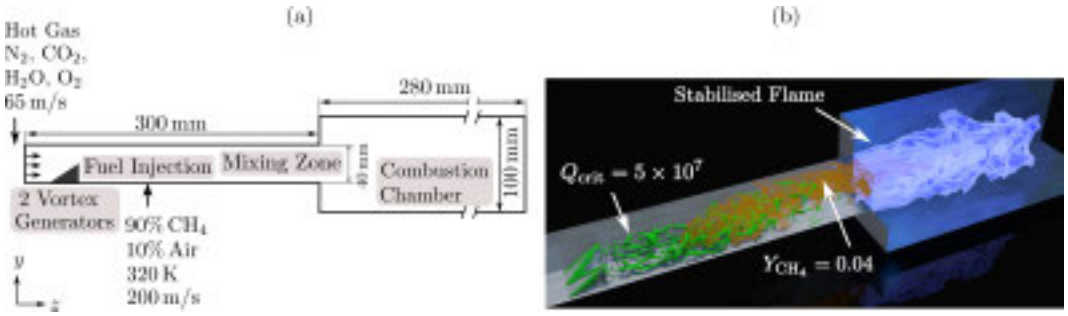

FIGURE 1. (a): Sketch of the simulated second stage sequential combustion system. (b): Instantaneous iso-contours of Q-criterion [28] (5×10^7), CH_4 mass fraction (0.04) and heat release rate (1×10^8 W/m^3). Atmospheric Pressure.

configuration: for example, decreasing the inlet temperature at 1 bar increases the flame length, while increasing the inlet temperature at 10 bar shortens it. Later in the paper it will be shown that at 10 bar autoignition is the dominant combustion regime. Assuming an inlet temperature of 1400 K instead of 1300 K at 10 bar autoignition times decrease by factor one third and the flame is expected to be located in the mixing zone, which is not acceptable. The effect of temperature difference is further discussed in the context of Fig. 6.

Fuel (methane/air at 320 K) is injected via jet in cross flow ($d_{\text{jet}} = 2.6$ mm) and the global equivalence ratio ϕ is fixed at 0.65. The hot gas and fuel mass flows are set to 23 g/s and 0.6 g/s (Thermal Power: 30 kW) at 1 bar, as well as 250 g/s and 6.0 g/s (300 kW) at 10 bar. The hot gas inlet has the following composition: $Y_{N_2} = 0.7405$, $Y_{O_2} = 0.1355$, $Y_{H_2O} = 0.056$ and $Y_{CO_2} = 0.068$. The authors are aware that NO_x can influence the oxidation of methane, as shown for example in [29]. For the present study the NO_x formation of the first stage is not considered.

Figure 1b shows iso-contours of the Q-criterion [28], CH_4 mass fraction and heat release rate Q. For the purpose of this study a pure jet in cross flow (jet-to-cross flow momentum ratio $J = (\rho_{\text{jet}} \cdot u_{\text{jet}}^2)/(\rho_{\text{cross}} \cdot u_{\text{cross}}^2) = 27$) configuration does not sufficiently mix fuel and hot gas. Therefore vortices are generated by 2 vortex generators ensuring an improved mixing between the two streams. At the inlet of the combustion chamber a flame is anchored due to hot products in the outer recirculation zone.

Numerical Methods

Compressible Large Eddy Simulation (LES) are performed with the explicit cell-vertex code AVBP [30] using the numerical scheme TTGC [31] with third order accuracy in space and time. The Smagorinsky approach was used to model subgrid Reynolds stress. Non-reflecting Navier-Stokes Characteristic Boundary Conditions [32] are imposed at the inlets and outlet. The heat loss formulation $\dot{q} = (T_{wall} - T_\infty)/R_{\text{w}}$ is applied to the domain walls. At atmospheric pressure the thermal resistance R_{w} is set to 0.02 K m^2/W in the mixing zone and 0.04 K m^2/W in the combustion chamber. At 10 bar R_{w} is decreased to 0.005 K m^2/W and 0.01 K m^2/W respectively. 2-D wall resolved simulations with characteristic velocities, pressure and temperatures show that these R_{w} result in wall temperatures of 700 K in the mixing zone and 1000 K in the combustion chamber. Heat losses decrease mixing temperatures, nevertheless wall temperatures are similar at 1 and 10 bar allowing a comparison of both cases.

Simulations were performed on an unstructured mesh with 1.9 million nodes (11.1 million cells) and a characteristic cell size of 0.7 mm in the reaction zone. The wall boundary layer is not resolved, which is compensated by a coupled velocity/temperature wall-model [33].

The Dynamic Thickened Flame (DTF) Model [34] was used for turbulent combustion modelling. The flame front is thickened to have a minimum of 4.5 cells inside the flame front allowing to resolve it on the LES grid and maintaining the correct laminar flame speed. At atmospheric pressure this results in thickening factors of approximately 9. The DTF model has not yet been applied to pure autoignition flame fronts as they appear at 10 bar. As shown in the upper part of Fig. 2 the flame position only depends on the autoignition time τ_{AI} and the inlet velocity u. The inlet velocity u also affects the flame thickness: A decreased u decreases the flame thickness and vice versa. One can imagine a homogeneous mixture transported in physical space: for the same mixture chemistry time scales stay constant, whereas the transport time scales change with u. With a minimum velocity of 10 m/s and therefore a flame thickness δ_x of 0.3 mm (compare with Fig. 2) a maximum thickening factor of 13 is obtained at 10 bar. Here the reader should note that a velocity of 10 m/s is chosen conservatively and represents the worst case. As shown later in the paper velocities close to the centre line reach easily 60 m/s and therefore thickening factors smaller than 13 are obtained. One can also refer to [22] for an application of the DTF to the Cabra flame configuration.

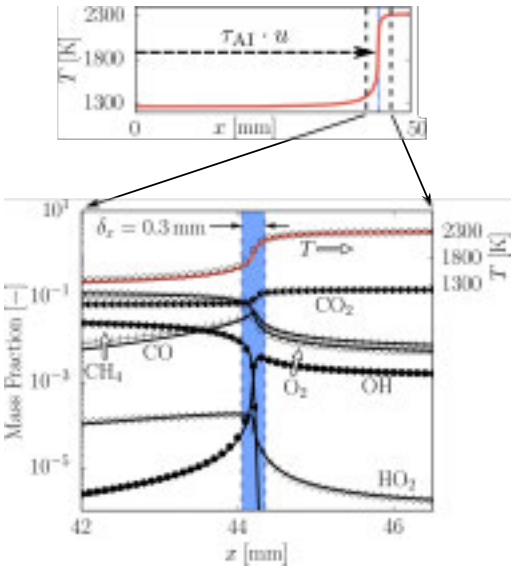

FIGURE 2. Profiles of temperature and mass fractions of a stoichiometric 1-D autoignition flame at 10 bar. Width of blue region highlights flame thickness δ_x. Top: Temperature profile with autoignition length $\tau_{AI} \cdot u$. Bottom: Zoom into flame region with profiles of temperature and mass fractions derived from detailed (lines) and reduced chemistry scheme ARC_16_10BAR_GRI30 (symbols).

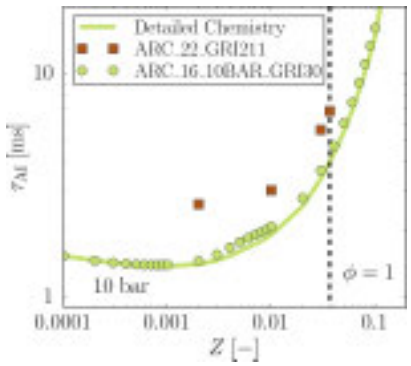

FIGURE 3. Autoignition time τ_{AI} over mixture fraction Z [38] for detailed and reduced chemistry schemes at 10 bar. Results derived from Perfectly Stirred Reactor (PSR) simulations.

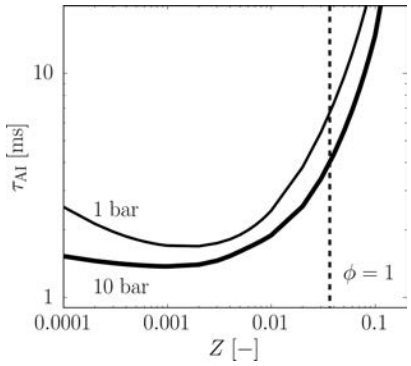

FIGURE 4. Autoignition time τ_{AI} over mixture fraction Z [38] for 1 bar and 10 bar. Stoichiometric mixture fraction $Z_{\phi=1} = 0.0365$. Results derived from Perfectly Stirred Reactor (PSR) simulations.

Analytically Reduced Chemistry

In the 1 bar simulations the analytically reduced chemistry (ARC) scheme ARC_22_GRI211 with 22 transported species is used. For a detailed validation of the scheme the reader is referred to [22, 35].

The ARC scheme for 10 bar is obtained from the detailed GRI-MECH 3.0 mechanism [36]. For this study NO_x prediction is not of interest and therefore 17 species involved in the NO_x pathways, namely: N, NO, N_2O, NO_2, NH, HNO, NH_2, NNH, CN, NCO, HCN, HOCN, HNCO, H_2CN, HCN, HCNO and NH_3 were removed in a first reduction step. At this stage the error for autoignition times obtained by Perfectly Stirred Reactor (PSR) simulations is less than 1%. In a second reduction step the following 12 species were removed using the directed relation graph with error propagation (DRGEP) method [37]: C, CH, C_2H_2, C_2H, HCCO, CH_2CO, CH_2OH, HCCOH, CH_2CHO, C_3H_7, CH_3CHO, C_3H_8 and AR. In the last reduction step the species HCNN, CH_2GSG-CH_2, CH_3O, HCO, CH_2, C_2H_5, H_2O_2 and C_2H_3 were identified suitable for quasi-steady state (QSS) assumption with analytical expressions of their concentrations [37]. Hence only the following 16 transported species remain in the scheme, named ARC_16_10BAR_GRI30: N_2, H, H_2, O, OH, O_2, H_2O, HO_2, CH_3, CH_2O, CO_2, CO, CH_3OH, CH_4, C_2H_6 and C_2H_4.

Profiles of temperature and species mass fractions for a 1-D autoignition flame derived using AVBP with ARC_16_10BAR_GRI30, as well as CANTERA with detailed chemistry are shown in Fig. 2. For the AVBP simulation (symbols) the inlet velocity u is set to 10 m/s. With $\tau_{AI} = 4.4$ ms this results in an autoignition length of $\tau_{AI} \cdot u = 44$ mm. For the CANTERA simulation u is increased to 10.8 m/s compensating an error in autoignition time of 8%. Profiles for temperature and species mass fractions are in excellent agreement.

Autoignition times τ_{AI} from PSR simulations at 10 bar for the two reduced schemes in comparison with GRI-MECH 3.0 are presented in Figure 3. In this study τ_{AI} is taken at maximum temperature gradient. ARC_22_GRI211 is not able to predict autoignition times correctly whereas the maximum error using ARC_16_10BAR_GRI30 is less than 10% which was considered acceptable for this study.

As shown in [35] including NO_x chemistry will result into 9 additional QSS species and 4 additional transported species, the latter one increasing computational cost by approximately factor 1.2.

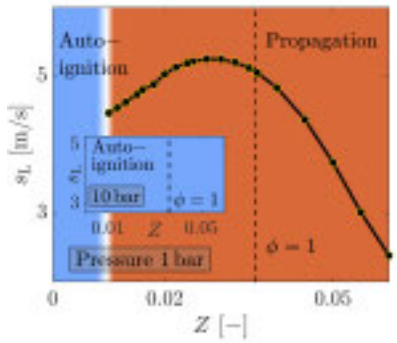

FIGURE 5. Laminar flame speed s_L over mixture fraction Z [38] for 1 bar. Derived from 1-D propagating premixed flame simulations (symbols). Propagating flames are observed up to $Z = 0.01$ (orange region). Blue regions are driven by autoignition and a freely propagating flame is not observed. Unburned gas temperature $T_u = 1409$ K. Inset plot: At 10 bar only autoignition flames are observed. $T_u = 1264$ K.

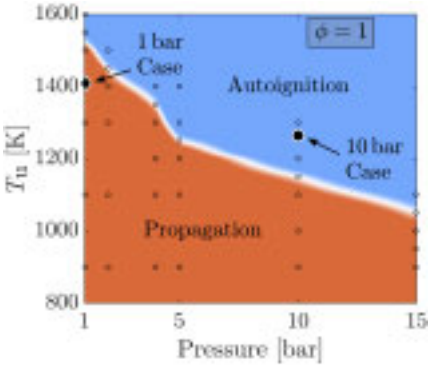

FIGURE 6. Transition from propagation (orange) to autoignition (blue) over a wide range of unburned gas temperature T_u and pressure at stoichiometric conditions. Open circles show simulated 1-D propagating and 1-D autoignition flames. Background colour from linear interpolation of simulaions (circles).

THE ROLE OF AUTOIGNITON AND PROPAGATION FROM 1 TO 10 BAR

Figure 4 shows the autoignition time τ_{AI} over mixture fraction Z for 1 bar and 10 bar computed with PSR simulations. Throughout the paper the mixture fraction definition by Bilger et al. [38] is used. Note that at 10 bar the hot gas cross flow temperature was decreased to 1300 K compensating the decrease of τ_{AI} with increased pressure, whereas the species composition is kept constant. The most reactive mixture fraction Z_{mr} defined at minimum τ_{AI} is found on the very lean side: $Z_{mr,1bar} \approx 0.002$ corresponding to an equivalence ratio of $\phi_{mr,1bar} \approx 0.053$ and $Z_{mr,10bar} \approx 0.001$ corresponding to $\phi_{mr,10bar} \approx 0.027$.

The laminar flame speed s_L over mixture fraction Z derived from 1-D propagating premixed flame simulations at 1 bar is shown in Fig. 5 (highlighted in orange). Below $Z_{trans} \approx 0.01$ (subscript trans denotes transitional) corresponding to $\phi_{trans} \approx 0.27$ freely propagating flames cannot be observed anymore and autoignition of the mixture starts to dominate (in blue). Similar observations were shown for the Cabra configuration in [22, 25]. At 10 bar (inset plot) mixture fractions are governed only by autoignition. Note that Z_{trans} is shifted to higher mixture fractions (≈ 0.2) larger than the maximum mixture fraction in the sequential burner just upstream of the flame ($Z_{max} \approx 0.04$) and is therefore not of interest for this study.

In Fig. 6 the transition from propagation to autoignition at stoichiometry ($\phi = 1$) is presented over a wide range of unburned gas temperature T_u and pressure. The composition was kept constant and corresponds to stoichiometry or $Z_{\phi=1} = 0.0365$. Note that in the sequential burner going from 1 to 10 bar the inlet hot gas temperature is decreased resulting in stoichiometric mixing temperatures of 1409 K and 1264 K respectively (both are marked in Fig. 6). Open circles represent 1-D propagating flame (in orange area), as well as 1-D autoignition flame (in blue area) simulations with CANTERA. The reader should note, that these data are not obtained using the autoignition index AI [22], which is introduced later in the paper. For a constant pressure the temperature is increased until a freely propagating flame is not observed anymore. This temperature marks the transition between propagation and autoignition, which is similar to the approach in Fig. 5, where the same phenomenon is investigated in mixture fraction space.

With increasing pressure one can observe the transition from propagation to autoignition at lower T_u. As shown for example in [17] laminar flame speeds s_L decrease with increasing pressure. For example, at $T_u = 1100$ K and 1 bar a 1-D propagation flame simulation with detailed chemistry gives $s_L = 1.96$ m/s. Increasing the pressure to 10 bar and keeping the same temperature (going in horizontal direction in Fig. 6) a propagating flame is till observed and s_L decreases to 0.64 m/s, which is agreement with $s_L \propto p^{1/2}$ [39]. A further increase of pressure (moving further in horizontal direction in Fig. 6) results in decreased autoignition times τ_{AI} and even lower s_L, hence a dynamic balance between flow velocity and flame propagation speed cannot be achieved anymore and autoignition starts to dominate. An increase in T_u (moving in upper vertical direction) increases laminar flame speeds [18], nevertheless τ_{AI} decreases and autoignition starts to dominate.

In the following the effect of different inlet temperatures T_{in} is discussed on the basis of Fig. 6. One can imagine a decrease of T_{in} at 1 bar and an increase of T_{in} at 10 bar to equal values. As a consequence the 1 bar case is shifted further down into the propagation region and the 10 bar case (both marked in Fig. 6) is shifted further up into the autoignition region. Indeed, when keeping the same mixture composition, higher temperatures promote autoignition and one can argue that the temperature difference does not change the conclusions drawn in the present study, but rather supports them.

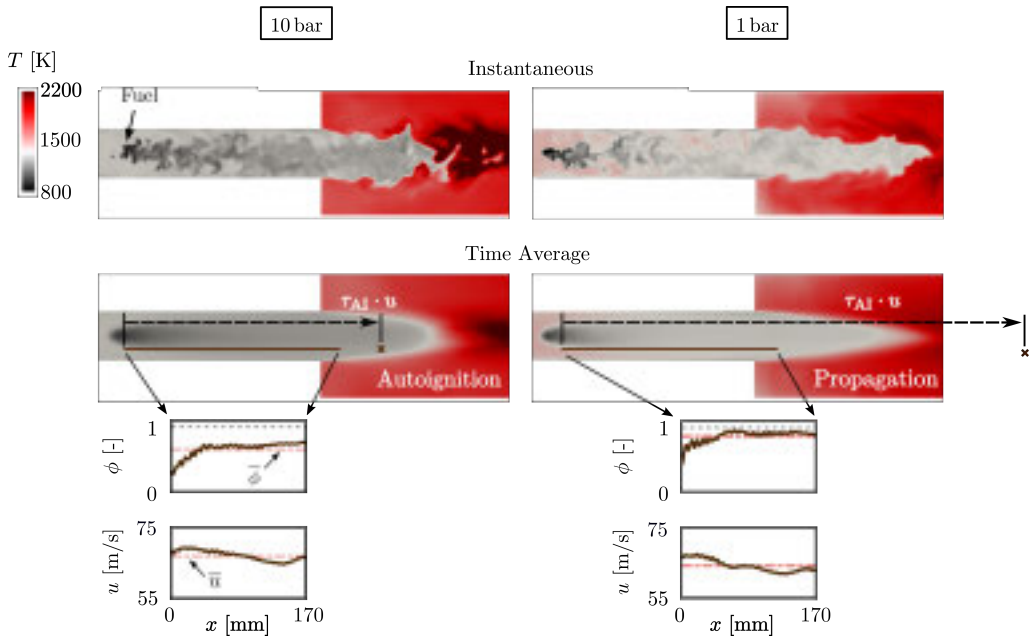

FIGURE 7. Horizontal cuts of instantaneous (top) and mean (bottom) temperature fields at 10 bar (left) and 1 bar (right). Plots with equivalence ratio ϕ and velocity u along axial lines are used to determine autoignition lengths $\tau_{AI} \cdot u$, with autoignition time τ_{AI} based on Perfectly Stirred Reactor (PSR) simulations.

COMPARISON OF FLAME ANCHORING MECHANISMS

Figure 7 compares instantaneous (top) and time averaged (bottom) temperature flow fields at 1 bar (right) and 10 bar (left). The horizontal y-cut is taken at half the height of the mixing zone and combustion chamber. At 10 bar the flame is more compact and one can observe an autoignition type flame shape being less conical compared to 1 bar. Here the reader is referred to compare with high pressure flame fields in [40–43]. With the aim of quantifying autoignition and propagating type flames time averaged velocities $\overline{u}$ and autoignition times τ_{AI} based on mixture compositions are extracted along an axial line for both simulations (brown lines, offset from centerline 12 mm). Along these lines compositions do not change significantly and a mixed state is assumed. The equivalence ratio ϕ and u, as well as $\overline{\phi}$ and $\overline{u}$ are plotted along the lines.

At 10 bar the time and spatially averaged equivalence ratio $\overline{\phi}$ is determined as 0.66, which corresponds to a mixture fraction Z of 0.0245 and an autoignition time τ_{AI} of 2.9 ms computed with a PSR simulation (compare with Fig. 4). With an averaged velocity $\overline{u}$ of 67.1 m/s the autoignition length is determined as $\tau_{AI} \cdot \overline{u} = 195$ mm and is marked with a brown cross, which matches well with the average flame position at 10 bar. Although this is a complex 3-D configuration with strong turbulence chemistry interactions time scales from 0-D PSR simulations do not become meaningless and can be used to have a first guess on the autoignition length under the assumption that conditions along the path do not change significantly.

At atmospheric pressure (right part of Fig. 7) the same procedure is repeated. With $\overline{\phi} = 0.87$ ($Z = 0.032$) and a corresponding $\tau_{AI} = 5.8$ms, as well as $\overline{u} = 64.3$ m/s the theoretical autoignition length (373 mm) is located far downstream of the flame stabilisation position visualised by the cross outside the bottom averaged T field. The flame position cannot be determined using an autoignition length which indicates that it is mainly driven by propagation. At this height the flame changes from an autoignition flame to a mainly propagating driven type flame when decreasing pressure from 10 to 1 bar, which is in agreement with findings in Fig. 5.

The above statement is made from an "autoignition point of view". It shows that the 10 bar case is autoignition driven and the 1 bar case is not. In the following it will be shown that a "propagation point of view" gives the same results. The stoichiometric laminar flame speed at 1 bar is computed as $s_L = 5.1$ m/s. With $s_T/s_L \approx 1 + u'/s_L$ [44] the turbulent flame speed has an estimated value of 11 m/s. The rms velocity $u' = 6$ m/s is extracted in the central heat release zone. With a decrease in temperature of 150 K (as it is done at 10 bar) s_L decreases to 3.3 m/s and therefore the turbulent flame speed drops to 9.3 m/s using the same u'. In the following we could imagine a propagating type flame at 10 bar. It is assumed that the turbulent flame speed is pressure independent [19]. Hence at 10 bar a turbulent flame speed of 9.3 m/s would result in a stretched flame with a flame tip located further downstream compared to 1 bar or even in flame blow off. However the opposite trend is observed: the flame is more compact, which suggests that the driving mechanism is autoignition.

Figure 8 shows scatter plots of scalar dissipation rate χ against

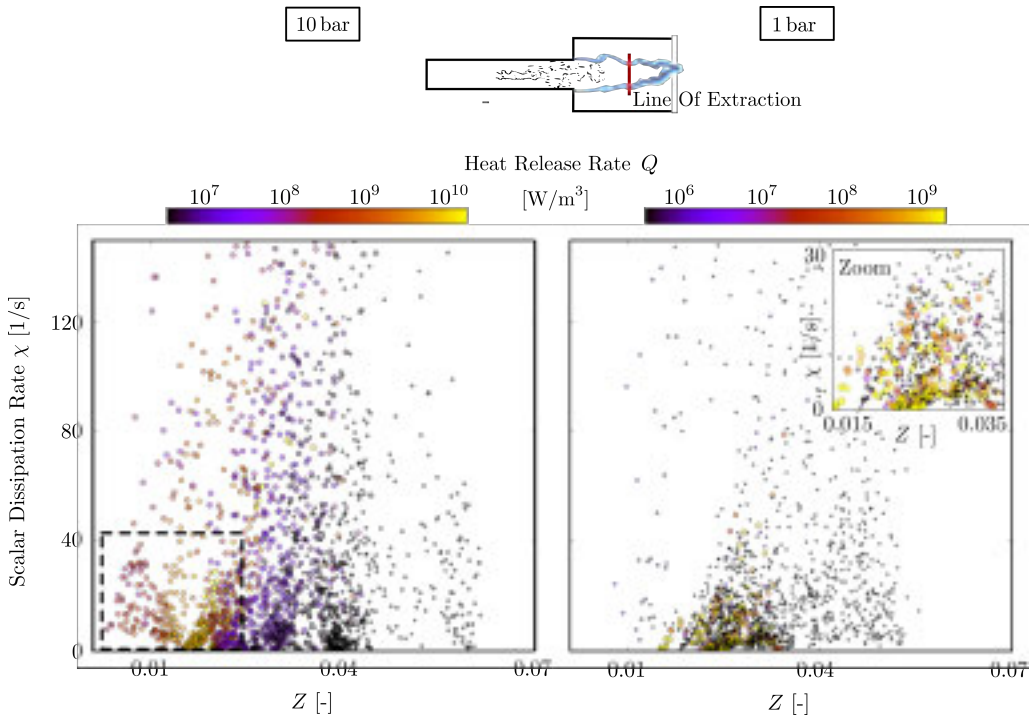

FIGURE 8. Scatter plots showing scalar dissipation rate χ against mixture fraction Z [38] coloured by heat release rate Q at 10 bar (left) and 1 bar (right). Data extracted at horizontal y-line at half the height of the combustion chamber (red line in sketch). Scatter conditioned on $Y_{CH_4} > 1 \times 10^{-5}$ to disregard post-flame chemistry. Dashed square in left plot marks region favourable for autoignition (low Z and low χ) where no point with low Q (black) are observed. Scatter size as function of heat release rate Q: large for $Q > 1 \times 10^7$, medium for $1 \times 10^7 > Q > 1 \times 10^6$ and small for $Q < 1 \times 10^6$.

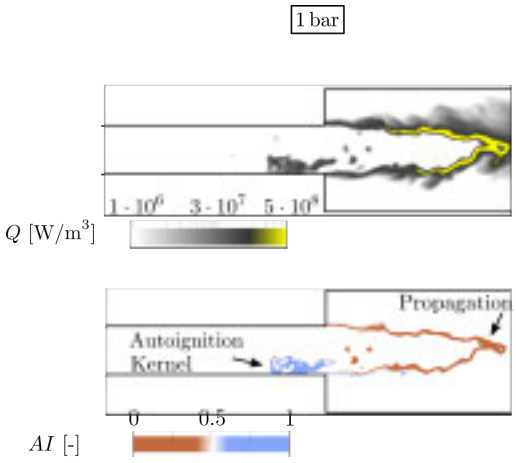

FIGURE 9. Instantaneous flow fields of heat release rate Q (top) in logarithmic scale and autoignition index AI [22] (bottom) on a horizontal y-cut. Blue regions correspond to autoignition ($AI > 0.5$) and orange regions to propagation ($AI < 0.5$).

mixture fraction Z coloured by heat release rate Q at 10 bar (left) and 1 bar (right). χ is defined as

$$\chi = \frac{1}{Sc}\left[\left(\frac{\partial Z}{\partial x}\right)^2 + \left(\frac{\partial Z}{\partial y}\right)^2 + \left(\frac{\partial Z}{\partial z}\right)^2\right] \tag{1}$$

with Schmidt number Sc. As shown in the sketch data are extracted along a horizontal y-line at half the height of the combustion chamber. Only points with $Y_{CH_4} > 1 \times 10^{-5}$ are considered, which allows to focus on reaction regions in the bulk flow and the flame without post-flame chemistry. As shown in [45] turbulent autoignition is observed when mixture fractions are close to the most reactive one and when the conditional scalar dissipation rates $\chi|_{Z_{mr}}$ (mr stands for most reactive) are low. In Fig. 8 it is shown that mixture fractions at this axial position range between approximately $0.008 < Z < 0.065$ for both pressures, which is due to mixing effects. Therefore Z are larger than the most reactive ones ranging between $0.0008 < Z_{mr} < 0.003$ for 10 bar and $0.001 < Z_{mr} < 0.004$ for 1 bar (compare with Fig. 4). Nevertheless autoignition is expected to be favourable at low autoignition times and therefore low mixture fractions, here denoted as Z_{low}, as well as low conditional scalar dissipation rates $\chi|_{Z_{low}}$. Indeed, as shown in the left part of Fig. 8, at 10 bar most of the points with large Q are located at low Z and low χ. One can also see that once favourable conditions for autoignition are reached, heat is

always released and there are even regions where no scatter with low Q (black dots) are observed anymore (marked by the dashed square). In contrary, at 1 bar (right plot and inset with zoom) points with low Q are observed over the whole Z range, even at conditions favourable for autoignition. This is a strong indication that here autoignition is not the driving combustion regime, which is in agreement with the above observations.

Previous results indicate propagation as the dominant combustion regime at 1 bar. Nevertheless as seen in Fig. 5 autoignition type flames can occur at lower mixture fractions, which is visualised in Fig. 9 showing instantaneous heat release rate Q in logarithmic scale (top) and the autoignition index AI [22] (bottom). AI allows to distinguish between autoignition and propagation based on the relative contribution of two reactions for hydroperoxyl (HO_2) consumption:

$$AI = \left| \frac{\dot{\omega}_{HO_2}^{(R8)}}{\dot{\omega}_{HO_2}^{(R8)} + \dot{\omega}_{HO_2}^{(R6)}} \right|, \tag{2}$$

with HO_2 reaction rates $\dot{\omega}_{HO_2}$ for the following two reactions (same numbering as in [22] and [27]):

$$HO_2 + H \Longleftrightarrow OH + OH \tag{R6}$$

$$HO_2 + OH \Longleftrightarrow H_2O + O_2. \tag{R8}$$

For $AI > 0.5$, HO_2 reaction rates of R8 locally dominate over the ones of R6 and an autoignition burning regime is identified; propagation is detected for $AI < 0.5$. A 1-D propagating flame simulation (not shown here) at 1 bar and $Z = 0.01$ was performed to validate the autoignition index. AI is extracted at maximum heat release rate Q and a value of 0.5 is obtained. Hence, the index predicts properly the transition between autoignition and propagation, which, as shown in Fig. 5, is located at $Z = 0.01$. In the present turbulent configuration AI is conditioned on Q and CH_2O (as done in [22]) allowing to include the autoignition kernel, but not the post flame chemistry. CH_2O is present during initialisation of autoignition and drops with high temperature chemistry [27]. In Fig. 9 an autoignition kernel with relatively low Q is located inside the mixing zone close to the wall and gets convected downstream. One can also see a thin autoignition region close to the lower rim. However the stabilised flame is mainly driven by propagation especially in regions with high Q coloured in yellow, which is in agreement with results in Fig. 7. Note that AI is not valid at high pressure and therefore cannot be used in the 10 bar case. As shown for example in [46] dominant reactions change compared to atmospheric pressure and AI needs to be redefined for high pressure.

CONCLUSIONS AND OUTLOOK

In the present paper the combustion regimes of a sequential combustor are investigated at atmospheric and high pressure. Flame propagation is identified as the dominant mechanism at 1 bar. An analysis of the average flow field mixing zone shows that autoignition times from PSR simulations cannot be used to determine the flame front position. Nevertheless a study in mixture fraction space Z indicates that at low Z autoignition exists, which was shown in an instantaneous field using the autoignition index AI.

A mapping of temperature and pressure dependent transition between propagation and autoignition highlights that with increasing pressure autoignition starts to dominate at lower temperatures. At 10 bar autoignition is the dominant burning regime and flame anchoring mechanism. In the relevant mixture fraction space of the sequential configuration only autoignition regions are present. The mixing zone analysis illustrates that autoignition times from PSR can be used to have a first guess on the flame front position.

This work highlights the difference of the combustion regimes at low and high pressure conditions. Although both flames look qualitatively similar they are subject to very different combustion processes. In the scope of thermoacoustic instabilities future work should address the differences in flame response to flow perturbations. One could assume that propagating flames and autoignition flames show a different behaviour, especially for temperature fluctuations due to the non-linear dependence of the reaction rate on the temperature in the Arrhenius expression.

ACKNOWLEDGEMENT

This research is supported by the Swiss National Science Foundation under Grant 160579.

REFERENCES

[1] T. Poinsot, "Prediction and control of combustion instabilities in real engines," *Proc. Combust. Inst.*, vol. 36 (in press), 2016.

[2] T. C. Lieuwen and B. T. Zinn, *Combustion Instabilities: Basic Concepts*. 2005.

[3] N. Noiray and A. Denisov, "A method to identify thermoacoustic growth rates in combustion chambers from dynamic pressure time series," *Proc. Combust. Inst.*, vol. 36 (in press), 2016.

[4] K. Prieur, D. Durox, and T. Schuller, "A hysteresis phenomenon leading to spinning or standing azimuthal instabilities in an annular combustor," *Combust. Flame*, vol. (in press), 2016.

[5] S. Taamallah, S. J. Shanbhogue, and A. F. Ghoniem, "Turbulent flame stabilization modes in premixed swirl combustion: Physical mechanism and Karlovitz number-based criterion," *Combust. Flame*, vol. 166, pp. 19–33, 2016.

[6] N. A. Worth and J. R. Dawson, "Azimuthally forced flames in an annular combustor," *Proc. Combust. Inst.*, vol. 36, 2016.

[7] J. A. Wagner, S. W. Grib, M. W. Renfro, and B. M. Cetegen, "Flowfield measurements and flame stabilization of a premixed reacting jet in vitiated crossflow," *Proc. Combust. Inst.*, vol. 36 (in press), 2016.

[8] K. Oberleithner, S. Schimek, and C. O. Paschereit, "Shear flow instabilities in swirl-stabilized combustors and their impact on the amplitude dependent flame response: A linear stability analysis," *Combust. Flame*, vol. 162, no. 1, pp. 86–99, 2015.

[9] S. Terhaar, K. Oberleithner, and C. O. Paschereit, "Key parameters governing the precessing vortex core in reacting flows: An experimental and analytical study," *Proc. Combust. Inst.*, vol. 35, no. 3, pp. 3347–3354, 2015.

[10] G. Tautschnig, E. Haner, C. Hirsch, and T. Sattelmayer, "Experimental and numerical investigation of confined jets in how co-flow," in *ASME Turbo Expo*, pp. GT2014–25843, 2015.

[11] B. Ćosić, S. Terhaar, J. P. Moeck, and C. O. Paschereit, "Response of a swirl-stabilized flame to simultaneous perturbations in equivalence ratio and velocity at high oscillation amplitudes," *Combust. Flame*, vol. 162, pp. 1046–1062, 2014.

[12] R. Sullivan, B. Wilde, D. R. Noble, J. M. Seitzman, and T. C. Lieuwen, "Time-averaged characteristics of a reacting fuel jet in vitiated cross-flow," *Combust. Flame*, vol. 161, no. 7, pp. 1792–1803, 2014.

[13] F. Güthe, J. Hellat, and P. Flohr, "The Reheat Concept: The Proven Pathway to Ultralow Emissions and High Efficiency and Flexibility," *J. Eng. Gas Turbines Power*, vol. 131, no. 2, p. 021503, 2009.

[14] C. Prathap, F. C. C. Galeazzo, P. Kasabov, P. Habisreuther, N. Zarzalis, C. Beck, W. Krebs, and B. Wegner, "Analysis of NOX Formation in an Axially Staged Combustion System at Elevated Pressure Conditions," *J. Eng. Gas Turbines Power*, vol. 134, no. 3, p. 031507, 2012.

[15] T. Roediger, O. Lammel, M. Aigner, C. Beck, and W. Krebs, "Part-load operation of a piloted FLOX® combustion system," *J. Eng. Gas Turbines Power*, vol. 135, no. 3, pp. 1–12, 2013.

[16] S. Candel, D. Durox, T. Schuller, J.-F. Bourgouin, and J. P. Moeck, "Dynamics of swirling flames," *Annu. Rev. Fluid Mech.*, vol. 46, pp. 147–173, 2014.

[17] E. Ranzi, A. Frassoldati, R. Grana, A. Cuoci, T. Faravelli, A. P. Kelley, and C. K. Law, "Hierarchical and comparative kinetic modeling of laminar flame speeds of hydrocarbon and oxygenated fuels," *Prog. Energy Combust. Sci.*, vol. 38, no. 4, pp. 468–501, 2012.

[18] X. J. Gu, M. Z. Haq, M. Lawes, and R. Woolley, "Laminar burning velocity and Markstein lengths of methane-air mixtures," *Combust. Flame*, vol. 121, no. 1-2, pp. 41–58, 2000.

[19] P. Griebel, P. Siewert, and P. Jansohn, "Flame characteristics of turbulent lean premixed methane/air flames at high pressure: Turbulent flame speed and flame brush thickness," *Proc. Combust. Inst.*, vol. 31 II, no. x, pp. 3083–3090, 2007.

[20] R. Cabra, J. Y. Chen, R. W. Dibble, a. N. Karpetis, and R. S. Barlow, "Lifted methane-air jet flames in a vitiated coflow," *Combust. Flame*, vol. 143, no. 4, pp. 491–506, 2005.

[21] C. S. Yoo, R. Sankaran, and J. H. Chen, "Three-dimensional direct numerical simulation of a turbulent lifted hydrogen jet flame in heated coflow: flame stabilization and structure," *J. Fluid Mech.*, vol. 640, p. 453, 2009.

[22] O. Schulz, T. Jaravel, T. Poinsot, B. Cuenot, and N. Noiray, "A criterion to distinguish autoignition and propagation applied to a lifted methane-air jet flame," *Proc. Combust. Inst.*, vol. 36 (in press), 2016.

[23] S. Navarro-Martinez and a. Kronenburg, "LES-CMC simulations of a lifted methane flame," *Proc. Combust. Inst.*, vol. 32 I, pp. 1509–1516, 2009.

[24] M. Jangi, X. Zhao, D. C. Haworth, and X.-S. Bai, "Stabilization and liftoff length of a non-premixed methane/air jet flame discharging into a high-temperature environment: An accelerated transported PDF method," *Combust. Flame*, vol. 162, no. 2, pp. 408–419, 2015.

[25] P. Domingo, L. Vervisch, and D. Veynante, "Large-eddy simulation of a lifted methane jet flame in a vitiated coflow," *Combust. Flame*, vol. 152, no. 3, pp. 415–432, 2008.

[26] M. Ihme and Y. C. See, "Prediction of autoignition in a lifted methane/air flame using an unsteady flamelet/progress variable model," *Combust. Flame*, vol. 157, no. 10, pp. 1850–1862, 2010.

[27] K. Gkagkas and R. P. Lindstedt, "Transported PDF modelling with detailed chemistry of pre- and auto-ignition in CH4/air mixtures," *Proc. Combust. Inst.*, vol. 31 I, pp. 1559–1566, 2007.

[28] J. C. R. Hunt, a. a. Wray, and P. Moin, "Eddies, streams, and convergence zones in turbulent flows," *Cent. Turbul. Res. Proc. Summer Progr.*, no. 1970, pp. 193–208, 1988.

[29] P. Dagaut and A. Nicolle, "Experimental study and detailed kinetic modeling of the effect of exhaust gas on fuel combustion: Mutual sensitization of the oxidation of nitric oxide and methane over extended temperature and pressure ranges," *Combust. Flame*, vol. 140, no. 3, pp. 161–171, 2005.

[30] L. Y. M. Gicquel, N. Gourdain, J. F. Boussuge, H. Deniau, G. Staffelbach, P. Wolf, and T. Poinsot, "High performance parallel computing of flows in complex geometries," *Comptes Rendus - Mec.*, vol. 339, no. 2-3, pp. 104–124, 2011.

[31] O. Colin and M. Rudgyard, "Development of High-Order Taylor–Galerkin Schemes for LES," *J. Comput. Phys.*, vol. 162, no. 2, pp. 338–371, 2000.

[32] T. J. Poinsot and S. K. Lele, "Boundary conditions for di-

rect simulations of compressible viscous flows," *J. Comput. Phys.*, vol. 101, no. 1, pp. 104–129, 1992.

[33] E. R. Van Driest, "Turbulent boundary layer in compressible fluids," *J. Spacecr. Rockets*, vol. 40, no. 6, pp. 1012–1028, 2003.

[34] O. Colin, F. Ducros, D. Veynante, and T. Poinsot, "A thickened flame model for large eddy simulations of turbulent premixed combustion," *Phys. Fluids*, vol. 12, no. 7, pp. 1843–1863, 2000.

[35] T. Jaravel, E. Riber, B. Cuenot, and G. Bulat, "Large Eddy Simulation of a model gas turbine burner using reduced chemistry with accurate pollutant prediction," *Proc. Combust. Inst.*, vol. 36, 2016.

[36] Z. Q. Gregory P. Smith, David M. Golden, Michael Frenklach, Nigel W. Moriarty, Boris Eiteneer, Mikhail Goldenberg, C. Thomas Bowman, Ronald K. Hanson, Soonho Song, William C. Gardiner, Jr., Vitali V. Lissianski, "http://www.me.berkeley.edu/gri_mech/."

[37] P. Pepiot-Desjardins and H. Pitsch, "An efficient error-propagation-based reduction method for large chemical kinetic mechanisms," *Combust. Flame*, vol. 154, no. 1-2, pp. 67–81, 2008.

[38] R. W. Bilger, S. H. Starner, and R. J. Kee, "On reduced mechanisms for methane-air combustion in nonpremixed flames," *Combust. Flame*, vol. 80, no. 2, pp. 135–149, 1990.

[39] H. Kobayashi, T. Tamura, K. Maruta, and T. Niioka, "Burning velocity of turbulent premixed flames in a high pressure environment," *Proc. Combust. Inst.*, vol. 26, pp. 389–396, 1996.

[40] Y. Yang, N. Noiray, A. Scarpato, O. Schulz, K. M. Düsing, and M. Bothien, "Numerical analysis of the dynamic flame reponse in Alstom reheat combustion systems," in *ASME Turbo Expo*, pp. GT2015–42622, 2015.

[41] A. Scarpato, L. Zander, R. Kulkarni, and B. Schuermans, "Identification of multi-parameter flame transfer function for a reheat combustor," in *ASME Turbo Expo*, pp. GT2016–57699, 2016.

[42] M. Zellhuber, J. Schwing, B. Schuermans, T. Sattelmayer, and W. Polifke, "Experimental and numerical investigation of thermoacoustic sources related to high-frequency instabilities," *Int. J. Spray Combust. Dyn.*, vol. 6, no. 1, pp. 1–34, 2014.

[43] M. Zellhuber, C. Meraner, R. Kulkarni, W. Polifke, and B. Schuermans, "Large Eddy Simulation of Flame Response to Transverse Acoustic Excitation in a Model Reheat Combustor," *J. Eng. Gas Turbines Power*, vol. 135, no. 9, p. 091508, 2013.

[44] Ö. L. Gülder, "Turbulent premixed flame propagation models for different combustion regimes," *Proc. Combust. Inst.*, vol. 23, no. 1, pp. 743–750, 1991.

[45] E. Mastorakos, T. a. Baritaud, and T. J. Poinsot, "Numerical simulations of autoignition in turbulent mixing flows," *Combust. Flame*, vol. 109, no. 1-2, pp. 198–223, 1997.

[46] E. L. Petersen, D. M. Kalitan, S. Simmons, G. Bourque, H. J. Curran, and J. M. Simmie, "Methane/propane oxidation at high pressures: Experimental and detailed chemical kinetic modeling," *Proc. Combust. Inst.*, vol. 31 I, pp. 447–454, 2007.